Geodesic H-Plane Horn Antennas

Mingzheng Chen, *Student Member, IEEE*, Francisco Mesa, *Fellow, IEEE*,
and Oscar Quevedo-Teruel, *Fellow, IEEE*

Abstract— This article describes a detailed procedure that allows for a time-efficient design of fully metallic geodesic H-plane horn antennas using an in-house ray-tracing method together with an optimization algorithm. With all the propagation in the air, geodesic H-plane horn antennas are of low loss and highly efficient. The proposed geodesic H-plane horn antennas provide a new degree of freedom, the height profile, to alleviate phase errors, realizing high gains and aperture efficiencies. Optimizations are implemented to design the height profile for a given target, enabled by the highly accurate and time-efficient in-house ray-tracing model. To demonstrate the correctness and versatility of the proposed design procedure, two prototypes are manufactured with computerized numerical control (CNC) machining and compared to their planar counterparts, with the aim of a high increased gain and aperture efficiency, respectively. The prototypes maintain good frequency stability from 26 to 33 GHz, with sidelobe levels lower than -15 dB and return loss better than 15 dB. The first prototype improves the realized gain by over 5 dB compared to the reference horn, while the second prototype achieves an aperture efficiency of around 65% within the operating frequency band.

Index Terms— Aperture efficiency, geodesic antenna, H-plane, horn antenna, ray tracing, realized gain.

I. INTRODUCTION

WITH the rapid development of modern technology, higher frequency bands are being considered to increase the data rate of wireless communications. This includes a wide range of applications, including terrestrial and satellite communications, automotive radars, and surveillance systems. In these new high-frequency bands, there is a demand for high-performance and cost-effective beamforming devices. Printed circuit board phased arrays, a dominant solution in low-frequency bands, suffer high losses and cost when the operating frequencies are shifted to higher bands, especially millimeter waves and above. At such high frequencies, quasioptical beamformers, such as reflectors and lenses, have gained more attention as a promising low-cost alternative for highly directive antennas [1], [2]. With a bulky shape and limited scanning capabilities, reflectors have restricted application scenarios, such as radio telescopes. Lens antennas, with high directivity, wide scanning range, and low scan losses, are generally more flexible [3]. Among all types of lenses, geodesic lenses are especially attractive due to two prominent merits: low cost and high efficiency [4]. Geodesic lenses use the height profile of a parallel plate waveguide (PPW) to introduce physical path-length differences that emulate an equivalent graded refractive index [5]. Therefore, when implemented in a simple and fully metallic configuration using PPW structures, geodesic lenses are ideal for high-frequency applications, avoiding the losses of dielectric materials [4], [6].

Horn antennas, also simple and fully metallic, have the potential to act as high-efficiency beamformers at high frequencies. They are realized by employing metallic tapering (i.e., a horn) to match electromagnetic waves from a waveguide to free space. When the tapering is applied only to the H-plane, the antenna is called the H-plane sectoral horn antenna [7]. Compared to common pyramidal and conical horn antennas with bulky geometries, H-plane horn antennas with low profiles are especially useful in systems with space constraints. An intrinsic property of horn antennas is the difference in the path lengths of waves reaching the open-flared aperture, causing a phase variation in the opening of the horn [8]. When the difference is small enough compared to the operating wavelength, the directivity of the horn antenna increases with increasing flare angle and aperture. However, as the flare angle and aperture keep increasing, the phase difference between the aperture's edge and center is large enough to lower the directivity of the horn. This inherent limitation hinders horn antennas from becoming highly directive beamformers.

There is extensive literature on how to alleviate this problem in H-plane horn antennas. The proposed methods can be classified according to whether the modification of phase distributions is performed outside or inside the horn antennas. In the first case, a component, such as a metal or dielectric lens, is placed in front of the aperture to control the emitted electromagnetic waves, which inevitably increases the footprint of the structure [9], [10], [11], [12], [13]. In the second case, the geometric characteristics of the horns are modified [14], [15] or additional structures, such as graded-index dielectric materials [16], [17], corrugations [18], and metal vias [19], [20], [21], are applied inside the horns. Most of the work in this second category is based on substrate-integrated waveguide technology or the use of graded-index dielectric materials, which suffer high dielectric losses at high frequencies.
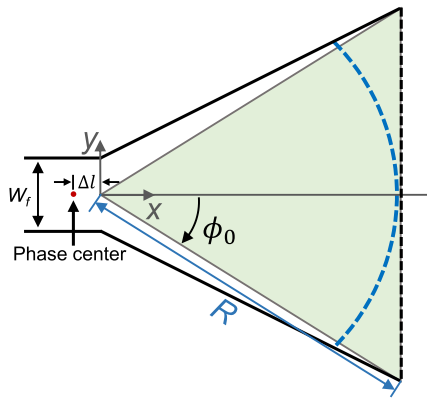
Fig. 1.   Top view of the geometry of an H-plane horn antenna.

Fully metallic H-plane horn antennas loaded with slow-wave metal structures, typically pins, are an alternative [22], [23]. Apart from the above-mentioned techniques, some full-wave numerical algorithms, such as the bodies of revolution finite-difference time-domain (BoR-FDTD) technique [24], [25], [26], can be applied to design and characterize H-plane horn antennas. However, these full-wave algorithms typically demand high computational resources.

To overcome some of these drawbacks, we propose the novel concept of fully metallic geodesic H-plane horn antennas, as well as a generic approach to design these antennas using an in-house ray-tracing (RT) method. The height profile of the H-plane horn antennas is carefully designed to control the path lengths of waves that arrive at different positions in the aperture. A general approach to the design and optimization of this geometrically complex profile is elusive with commercial full-wave simulators. In this article, the profile is designed and optimized using an in-house RT tool, which is time-efficient and reasonably accurate [27], [28]. Two prototypes are manufactured and measured to serve as experimental validation. The first design aims to minimize size while achieving an increase in gain. The second design aims to maximize aperture efficiency.

This article is organized as follows. In Section II, we propose an RT model to analyze H-plane horn antennas. This model is validated with full-wave simulations. In Section III, the RT model is used to design the height profile of two geodesic H-plane horn antennas working at the K$_a$-band. The experimental verification of these designs is also reported in this section. Finally, some conclusions are drawn in Section IV.

II. RAY-TRACING MODEL OF H-PLANE HORN ANTENNAS

A. Ray-Tracing Model

The geometry of an H-plane horn antenna is determined by three parameters: R, ϕ_0, and W_f, as illustrated in Fig. 1, assuming a constant height h for the feeding waveguide and the horn. W_f is the width of the waveguide, while R and ϕ_0 define a triangular zone on the horn marked green in Fig. 1. The blue dashed curve in Fig. 1 represents the cylindrical wavefront that arrives at the aperture of the horn, indicating an inevitable phase error [8]. In this configuration, the propagation of waves in H-plane horn antennas gradually transforms from the transverse electric$_{10}$ (TE$_{10}$) mode in the feed to the
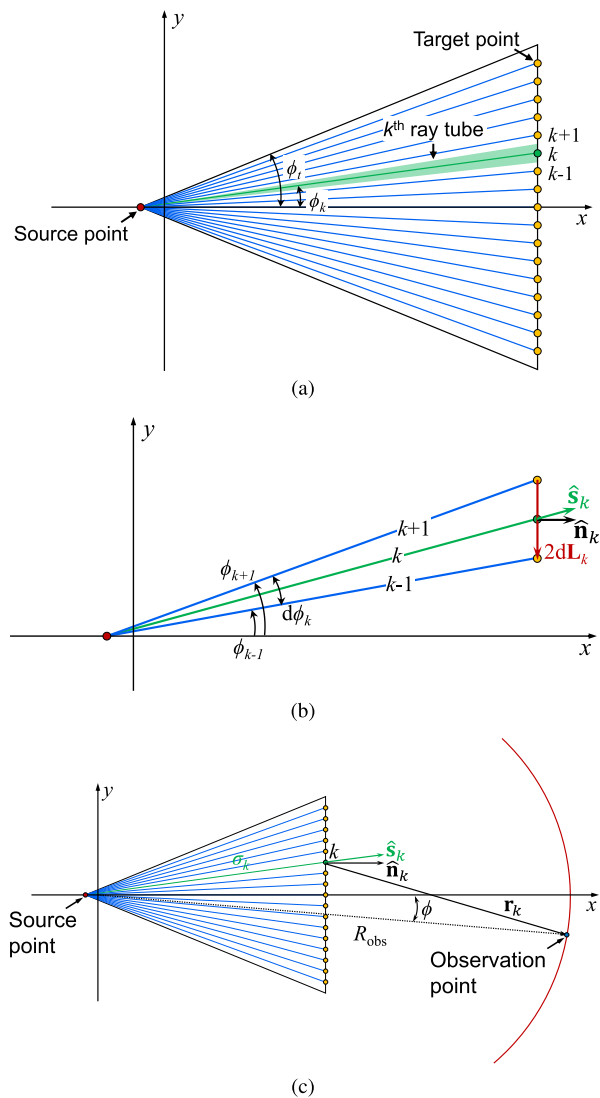

Fig. 2.   (a) Projections in the xy-plane of the geodesics in an H-plane horn antenna with a source point located at the phase center. (b) kth ray tube to evaluate the field amplitude in the aperture. (c) Geometric parameters to evaluate the far-field pattern.

transverse electromagnetic (TEM) mode in the aperture [7]. This assumes that the height h of the H-plane horn antenna is small enough compared to the operating wavelength to support only the fundamental mode. Commercial full-wave solvers are usually employed to simulate wave propagation inside the horn and to find the resulting radiation patterns. However, these simulations require large computing resources and long times. Recently, RT techniques have been shown to be an alternative considerably more time-efficient and sufficiently accurate for analyzing geodesic lenses [27], [28], [29], [30], [31], [32], [33]. Here, we adapt the numerical RT method proposed in [28] to evaluate H-plane horn antennas. As detailed in [28], this RT method can be described in the following steps.

1) Calculation of ray trajectories, or geodesics, traveling from the source point to any point in the aperture, as presented in Fig. 2(a). The source point is located at the phase center of the horn antenna.

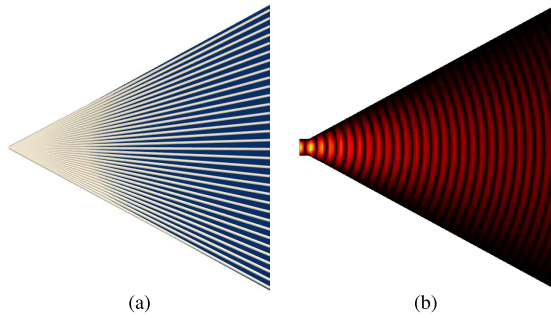2) Evaluation of the phase distribution of the E-field in the aperture using the length of the obtained geodesics.

Fig. 3. (a) Geodesics and (b) E-field distribution of an H-plane horn antenna at 30 GHz, with design parameters $R = 15\lambda$ and $\phi_0 = 30°$.

3) Obtaining the amplitude distribution of the E-field in the aperture using the ray-tube power conservation theory and the geometric parameters shown in Fig. 2(a) and (b).

4) Computation of the far-field radiation pattern using Kirchhoff's scalar diffraction theory in the geometry illustrated in Fig. 2(c).

Note that the parameters defined in Fig. 2 are the same as in [28]. In the RT model, the source point is displaced by Δl from the origin to coincide with the phase center. This displacement needs to be precisely defined and finely adjusted in the RT model to obtain a very good match of the RT results with full-wave simulations. Furthermore, the approximation of the feed model has a great influence on the accuracy of the amplitude distribution of the E-field in the horn aperture, which will be discussed later with specific design examples.

B. Model Validation

To validate the RT method outlined above, we compare the numerical results obtained using the RT method to full-wave simulations computed with the commercial software CST, which has proven to agree well with experimental results and is therefore used here as a benchmark. As a validation example, we use a planar H-plane horn antenna with design parameters $\phi_0 = 30°$ and $R = 150$ mm, which corresponds to 15λ at the design frequency $f_0 = 30$ GHz. The height h of the horn is set to 2 mm, which is 0.2λ at 30 GHz, to ensure that higher-order modes do not propagate within the horn. A rectangular waveguide of width $W_f = 8.64$ mm is used to feed the H-plane horn antenna, which corresponds to the dimension of the standard WR-34 appropriate for K_a-band designs. This specific waveguide feed is also employed in other designs in this work. Full-wave simulations are used to calibrate the feed model. In this planar case, a phase center displacement $\Delta l = 0.7\lambda$ inside the waveguide is adopted. Furthermore, the amplitude distribution (A'_k) of the waveguide feed model is approximated by a cosine function defined as $A'_k = \cos(\pi \phi_k / 2\phi_t)$, where ϕ_k is the angle of departure of the kth ray and ϕ_t is half the flare angle of the triangular zone considered in Fig. 2(a). In this configuration, we compute the geodesics of the H-plane horn antenna using the RT model and compare the results with the corresponding E-field distribution given by CST in Fig. 3. As expected, the geodesics in Fig. 3(a) are straight lines that come out radially from the source point (i.e., the phase center) to the horn aperture, which corresponds to the cylindrical wavefront of the E-field shown in Fig. 3(b).
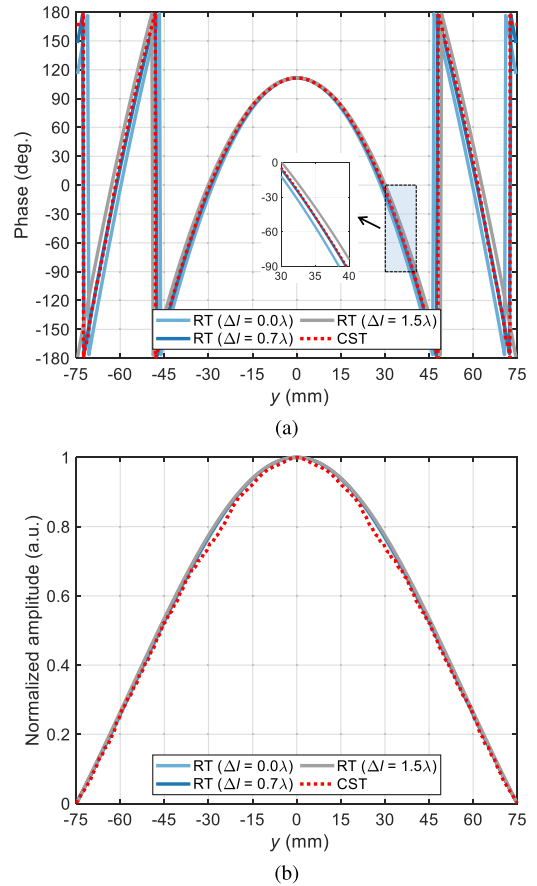

(a)

(b)

Fig. 4. (a) Phase and (b) normalized amplitude distributions of the E-field in the aperture of an H-plane horn antenna obtained from RT and CST at 30 GHz, with design parameters $R = 15\lambda$ and $\phi_0 = 30°$ and phase center displacement $\Delta l = 0.0\lambda$, 0.7λ, and 1.5λ.

Since impedance mismatch from the horn to free space is not considered in the RT model, open boundary conditions are applied in the CST model to the horn aperture, eliminating reflections. In the actual antenna design, a flared structure will be applied to ensure a smooth impedance transition in the horn aperture.

In the RT model, the length of the obtained rays is used to calculate the phase distribution of the E-field in the horn aperture, whereas the ray-tube theory provides information on the amplitude. The numerical RT and CST results of the phase and normalized amplitude distributions of the E-field at 30 GHz in the aperture of the H-plane horn are plotted in Fig. 4. With design parameters $R = 15\lambda$ and $\phi_0 = 30°$, the aperture size is also 15λ (150 mm). To illustrate the impact of the phase center displacement on the E-field distribution in the RT model, three different displacements $\Delta l = 0.0\lambda$, 0.7λ, and 1.5λ are considered. The results show that the displacement of the phase center mainly influences the phase distributions, while the amplitude distributions remain almost unchanged for different Δl. Therefore, a comparison of the results of the E-field phase distribution provided by the RT model in the horn aperture with the data obtained from CST is used to adjust the displacement of the phase center. In the present case, $\Delta l = 0.7\lambda$ is selected. With the adjusted phase center, very good agreement is found in both Fig. 4(a) and (b), with the small discrepancies in the amplitude distribution
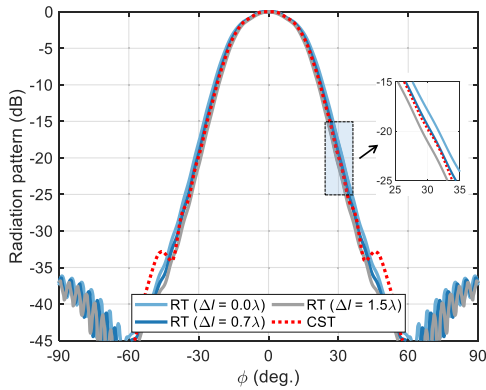
Fig. 5. Radiation patterns of an H-plane horn antenna obtained from RT and CST at 30 GHz, with design parameters $R = 15\lambda$ and $\phi_0 = 30°$ and phase center displacement $\Delta l = 0.0\lambda$, 0.7λ, and 1.5λ.

mainly attributed to the approximation errors of the amplitude distribution for the waveguide excitation.

Knowing the E-field distributions in the aperture provided by the RT model, we obtain the far-field radiation patterns using Kirchhoff's scalar diffraction theory. These results are compared to those obtained with the CST model in Fig. 5, showing very good agreement when the phase center is adjusted, particularly for the beamwidth and beam slope of the overall beam shape. However, the RT results with different Δl demonstrate that the phase center displacement does not have a strong impact on the accuracy of the calculated radiation pattern, although a good choice of this parameter can further improve this accuracy. Despite minor discrepancies, these results validate the accuracy of the RT model for the analysis of H-plane horn antennas. Furthermore, in terms of computational times, the RT model takes only about 5 s to obtain accurate results, while the CST model needs 10 min for this specific case. Therefore, the proposed modeling approach has the potential to be used as an optimization tool, and Section III illustrates the application of this tool for design purposes.

III. GEODESIC H-PLANE HORN ANTENNAS

The investigation of geodesic lens antennas has recently grown due to their low loss when implemented in fully metallic configurations. The existing literature has focused mainly on rotationally symmetric lenses, which typically mimic the performance of generalized Luneburg lenses [34], [35], [36], [37], [38], [39]. These lens antennas are able to scan with multiple or steerable feedings with low scan losses.

Differently, here, we design two fixed-beam geodesic H-plane horn antennas using the proposed RT method. We define the geodesic surface as the mean surface between the upper and lower conductive plates of the H-plane horn. By designing the geodesic surface shape appropriately, we are able to reduce the path-length differences of rays inside the horn. In this work, we propose to search for the optimal geodesic surface shape for a specific H-plane horn using a limited-memory Broyden–Fletcher–Goldfarb–Shanno algorithm for bound constraints (L-BFGS-B) [40]. Two designs are discussed: one aimed at a high increase in gain (design I) and the other with a high aperture efficiency (design II). After
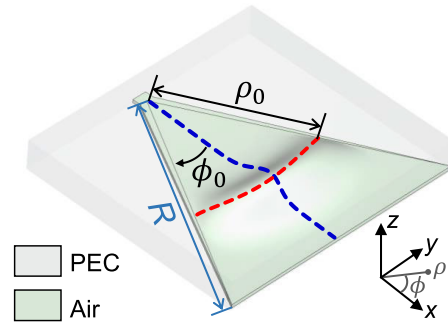

Fig. 6. Illustration of the geometry of a geodesic H-plane horn antenna.

obtaining the geodesic surface shapes, two realistic antenna prototypes are designed and measured to verify the design procedure.

A. Height Profile Design

The geometry of a geodesic H-plane horn antenna is depicted in Fig. 6, in which the green region represents an air channel between two parallel conductive plates made of a perfect electric conductor (PEC). The thickness of the channel is 2 mm, the same as the planar H-plane horn antenna treated in Section II-B. When the geodesic H-plane horn is oriented as in Fig. 6, the shape of the geodesic surface can be described by a height profile function of ρ and ϕ, that is, $z = f(\rho, \phi)$. Note that for a planar H-plane horn antenna, $z(\rho, \phi) = 0$.

The phase variation in the aperture of the H-plane horn is inherently caused by the path-length differences of rays traveling inside the horn. Due to the triangular geometry of the H-plane horn, the path length of the rays gradually increases from the center to the side of the horn ($|y| \le R \sin \phi_0$), which is also reflected in the phase variation presented in Fig. 4(a). As a result, to correct these path-length differences, the devised height profile makes use of the z-direction geometry, letting rays in the center of the horn propagate extra lengths compared to those in the sides. Furthermore, since the ray path-length differences are highly dependent on the particular configuration of the H-plane horn (R and ϕ_0), the height profile should also be adaptive for different H-plane horns.

Taking all of the above into account, we propose a height profile as

$$z(\rho, \phi) = A_h R \exp\left[-\left(\frac{\rho - \rho_0}{\eta}\right)^2\right]$$
$$\times \left[\left(\frac{\cos\left(\frac{\pi\phi}{\phi_0}\right) + 1 + \delta}{2}\right)^p - \left(\frac{\delta}{2}\right)^p\right] \quad (1)$$

in which R and ϕ_0 determine the basic geometry of an H-plane horn, while δ is a constant, and A_h, ρ_0, η, and p are the four parameters for optimization. The height profile has a Gaussian distribution along the ρ-direction and a quasicosine distribution along the angular ϕ-direction with a maximum of $z(\rho_0, 0) = A_h R [(1 + \delta/2)^p - (\delta/2)^p]$, as illustrated by the blue and red dashed lines in Fig. 6. Here, δ is a very small constant equal to 0.01 to avoid the numerical singularity 0^p
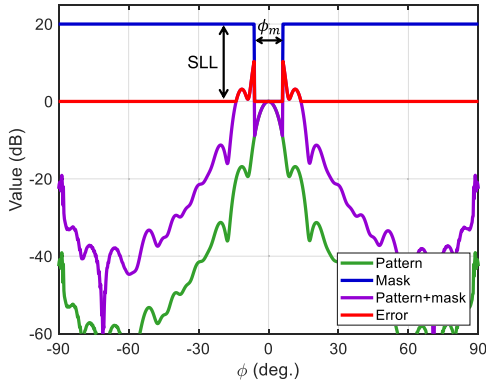
Fig. 7.   Example of the radiation pattern, mask, radiation pattern plus mask, and error in height profile optimization with design parameters $R = 15\lambda$ and $\phi_0 = 30°$ and optimization target SLL $= 20$ dB and $\phi_m = 12°$.

TABLE I

OPTIMIZED PARAMETERS FOR DESIGNS I AND II

Design	A_h	ρ_0	η	p
I	0.122152	0.603194	0.092725	0.278522
II	0.069242	0.725863	0.138455	0.226910

as $\phi \to \phi_0$. Other conditions imposed to the height profile are

$$\frac{\partial z(\rho = 0, \ \phi = 0)}{\partial \rho} \to 0 \qquad (2)$$

$$\frac{\partial z(\rho = \rho_0, \ \phi = \phi_0)}{\partial \phi} \to 0 \qquad (3)$$

$$\frac{\partial z(\rho = R \cos \phi_0, \ \phi = 0)}{\partial \phi} \to 0 \qquad (4)$$

with (2) and (3) required to ensure a smooth transition from the periphery to the geodesic surface so that the design can be physically implemented, and (4) in the horn aperture also needed to maintain good polarization purity. The specific profile given in (1) has been checked to be appropriate for the purpose of the present work. Other profiles could be more convenient if different radiation characteristics were targeted.

When using the RT approach to analyze geodesic H-plane horn antennas with the height profile defined by (1), two small modifications are needed for the assumptions made in Section II-B. The geodesic shape acts as a lens-like structure inside the H-plane horn, which has a focusing effect. As a result, it displaces the phase center and concentrates more field power to the middle part of the horn aperture. Using the phase distribution in the horn aperture obtained from the full-wave simulator as a reference, we can calibrate the phase center Δl. Furthermore, because more field power is in the middle part of the horn aperture for the geodesic case, we assume that the amplitude distribution follows the Gaussian profile already employed in [28]. In particular, using a profile similar to that in [28], the amplitude distribution is approximated as $A'_k = 10^{-(\phi_k/\phi_{3\text{dB}})^2/\xi} - 10^{-(\phi_t/\phi_{3\text{dB}})^2/\xi}$, where $\phi_{3\text{dB}}$ is the half-power beamwidth (HPBW) angle defined here (in degrees) as $\phi_{3\text{dB}} = \phi_t/2.77$, and $\xi = 50$. This modified waveguide excitation model is used in the geodesic H-plane horn designs in this article.

For a particular H-plane horn with design parameters R and ϕ_0, the L-BFGS-B method with the RT approach is used to optimize an optimal height profile. Note that many other

methods could be used with a similar result. Here, we choose an H-plane horn with $R = 15\lambda$ and $\phi_0 = 30°$ as an example to illustrate the potential of this method. As shown in Fig. 7, the blue line represents a mask function defined as

$$M(\phi) = \text{SLL}\left[1 - \text{rect}\left(\frac{\phi}{\phi_m}\right)\right] \qquad (5)$$

in which SLL is the required sidelobe level (in dB) and ϕ_m the sidelobe mask angle. The selection of SLL and ϕ_m depends on the geometry of the horn and the corresponding radiation patterns. In this example, SLL $= 20$ dB and $\phi_m = 12°$ are chosen. The green line in Fig. 7 is an example of an RT-calculated radiation pattern, $P(\phi)$, obtained with parameters $A_h = 0.12$, $\rho_0 = 0.6$, $\eta = 0.08$, and $p = 0.28$. We then define the error as $\mathcal{E}(\phi) = P(\phi) + M(\phi)$ when $P(\phi) + M(\phi) > 0$ and $\mathcal{E}(\phi) = 0$ otherwise. This error function is shown in red in Fig. 7. Finally, the target function to optimize is defined as

$$T = \sum_\phi \mathcal{E}(\phi) \qquad (6)$$

with the final goal of obtaining the minimal T. Other fitness functions could be used to achieve equivalent results. The study of the different optimization methods, as well as fitness functions, is beyond the scope of this article.

Since the optimal height profile depends on the particular geometry of the H-plane horn, for verification purposes, we select two specific designs that have practical applications. The design I has $R = 15\lambda$ and $\phi_0 = 30°$, the planar counterpart of which was used as the validation model in Section II-B. The merit of the planar configuration is its compactness with a small footprint. However, since the flare angle ϕ_0 is large, considerable phase variations occur in the planar horn aperture, resulting in low gain and aperture efficiency (less than 15%). By optimizing the height profile, resulting in the parameters shown in Table I, the design I can greatly increase the gain and aperture efficiency compared to the planar horn, while still maintaining its compactness. In comparison, the design II has design parameters of $R = 30\lambda$ and $\phi_0 = 12°$, making it relatively long and narrow-flared. As a result, the planar horn with this configuration already has a relatively high aperture efficiency. The purpose of design II is to further increase the aperture efficiency. The antenna sizes R are determined to realize a gain of around 20 dBi for both designs, considering a flare with a height of 10 mm for matching to free space, a question that will be discussed later.

After a few initial simulations, the phase center displacements are set to $\Delta l = 0.7\lambda$ for design I and $\Delta l = 1.5\lambda$ for design II. For both designs, a target sidelobe level of SLL $= 20$ dB and a mask angle of $\phi_m = 14.5°$ are defined. The mask angle specification is based on the actual aperture size of the horns and the initial simulation results. The resulting optimized parameters are listed in Table I, giving rise to the height profiles illustrated in Fig. 8. In particular, Fig. 8(a) presents the profiles along the ρ-axis with $\phi = 0°$ and Fig. 8(b) those along the ϕ-axis with $\rho = \rho_0$. The numerical results of both designs are reported in Figs. 9 and 10. Figs. 9(a) and 10(a) show the geodesics obtained using the RT model, while (b) depict the E-field distributions given by
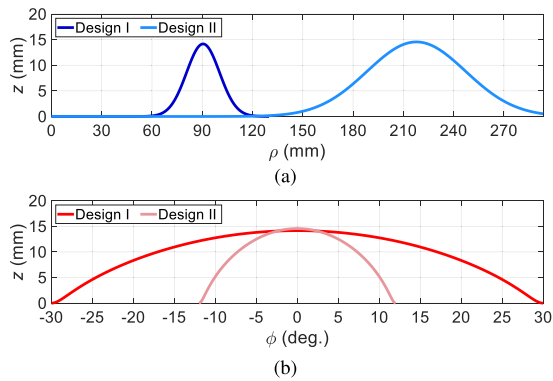
(a)

(b)

Fig. 8. Height profiles of the geodesic H-plane horn antennas along (a) ρ-axis when $\phi = 0°$ and (b) ϕ-axis when $\rho = \rho_0$.

(a)   (b)

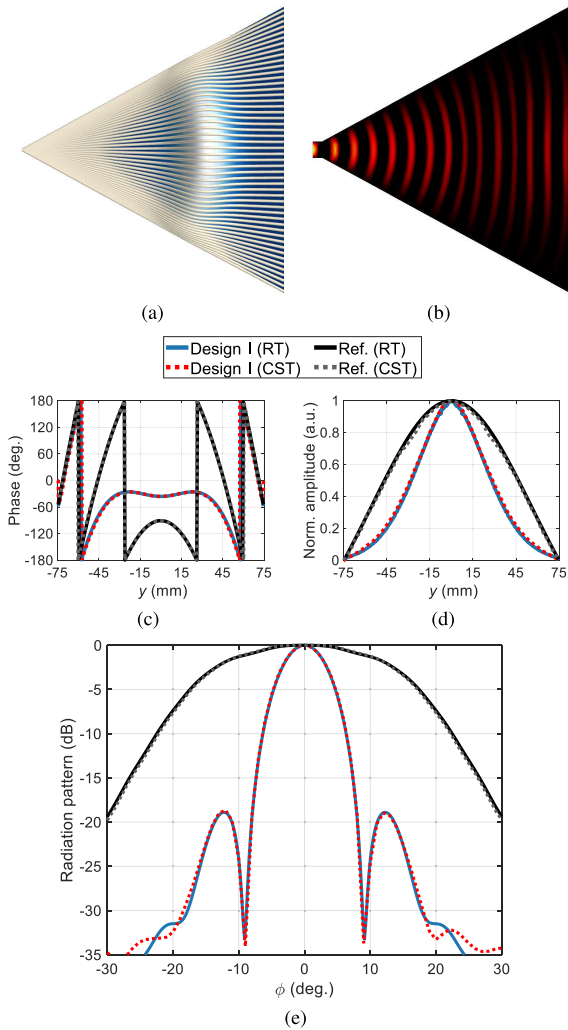(c)   (d)

(e)

Fig. 9. (a) Geodesics, (b) E-field distribution, (c) phase distribution of the E-field in the horn aperture, (d) normalized amplitude distribution of the E-field in the horn aperture, and (e) radiation patterns of design I at 30 GHz, with design parameters $R = 15\lambda$ and $\phi_0 = 30°$.

the full-wave simulator. The phase and normalized amplitude distributions of the E-field in the horn apertures are presented in Figs. 9(c) and (d) and 10(c) and (d), respectively. A comparison of the computed radiation patterns in the xy-plane are plotted in Figs. 9(e) and 10(e). A good collimation of rays can be observed in Figs. 9(a) and 10(a) for the geodesic horns as the rays arrive parallel at the horn aperture, particularly in the middle part, where the E-field power concentrates.
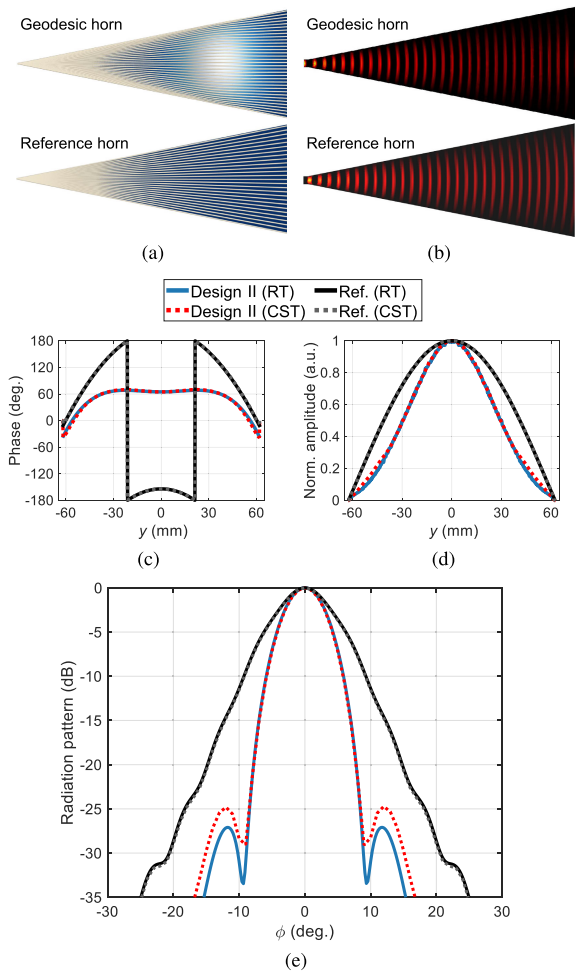

(a)   (b)

(c)   (d)

(e)

Fig. 10. (a) Geodesics, (b) E-field distribution, (c) phase distribution of the E-field in the horn aperture, (d) normalized amplitude distribution of the E-field in the horn aperture, and (e) radiation patterns of design II at 30 GHz, with design parameters $R = 30\lambda$ and $\phi_0 = 12°$.

The E-field distributions of the designs shown in Figs. 9(b) and 10(b) indicate that the cylindrical wavefront excited from the waveguide feed is gradually transformed into a planar wavefront on the horn aperture side compared to the reference horns. The geodesics and E-field distribution of the reference horn for the design I are presented in Fig. 3. After adjustment, the phase distributions in the horn aperture of the designs obtained from RT align well with the results from CST, as shown in Figs. 9(c) and 10(c). Moreover, the phase distributions of the designs in the middle part of the apertures are almost flat when the geodesic shapes are introduced, validating the correction effect of the phase errors. Regarding the amplitude distributions shown in Figs. 9(d) and 10(d), the results of the geodesic horns have a Gaussian distribution, compared to the cosine distribution of the reference horns. Accordingly, the amplitude distribution approximation of the waveguide feed in RT is modified for geodesic cases to align with the results of the full-wave simulation. The radiation patterns presented in Fig. 9(e) and 10(e) demonstrate excellent agreement in the shape of the main beam. A small discrepancy can be observed in the sidelobes of design II. However, the sidelobe level is already lower than -25 dB, so the differences are acceptable. Since the radiation patterns are normalized,

TABLE II
HPBW OF DESIGNS I AND II AND THEIR PLANAR REFERENCES AT 30 GHz

Design	Geo. (RT)	Geo. (CST)	Planar (RT)	Planar (CST)
I	7.4°	7.5°	28.8°	28.6°
II	6.7°	6.5°	8.6°	8.8°

we cannot directly obtain information on gain and aperture efficiency; HPBW of the main beam is used as an indicator here, as presented in Table II. As expected, design I realizes a great improvement compared to the planar reference horn, while design II has a smaller HPBW with a smaller aperture size than design I, which means a higher aperture efficiency. From an alternative viewpoint, compared to a planar H-plane horn with the same aperture size and aperture efficiency, design I can reduce the axial length (the shortest distance from the feed to the aperture) by a factor of approximately 4 (130 versus 524.7 mm) and design II by a factor of 2.5 (293.4 versus 747.4 mm).

In terms of computational complexity, [28] reported reduction factors above 40 and 2, respectively, for the CPU and memory cost of the proposed RT approach compared to simulations using commercial full-wave software. In our specific case of geodesic horn antennas, the computational time required for the RT method is less than 5 s, while the CST simulation needs 20 min for design I and 45 min for design II. Therefore, the time efficiency of the RT approach enables its use as a valuable design tool.

In summary, the height-profile design implemented consists of the following steps.

1) Assume a waveguide feed model with an initial value of Δl obtained from the planar horn for a particular H-plane horn with given R and ϕ_0.
2) Optimize a height profile defined by (1). Note that although we used the L-BFGS-B method for optimization here, many other methods could be employed.
3) Adjust the phase center Δl of the feed model using a full-wave model with a height profile obtained in Step 2.
4) Optimize the height profile with the calibrated waveguide feed model.

B. Antenna Design

Designs I and II described in Section III-A are first validated using CST, before manufacturing and measuring the prototypes. Therefore, additional components must be added to realistically model the structures, as presented in Fig. 11. To ensure that only the main mode can propagate, the thickness of the air cavity is set to 2 mm, meaning that matching areas are required on the port and aperture side. On the feeding side, a five-step cascade transition is designed to transform the height of 2 mm to 4.32 mm, with a total length of 16.2 mm. After the transition, the cross section of the waveguide feed is 8.64×4.32 mm, which is the dimension of the standard waveguide WR-34. Finally, a commercial WR-34 waveguide to coaxial adapter working from 22 to 33 GHz is used during the measurement. On the aperture side, a flare with a sinusoidal shape of 2–10 mm in height and a length of 18 mm is used to ensure a good match from the horn antenna to the free space.
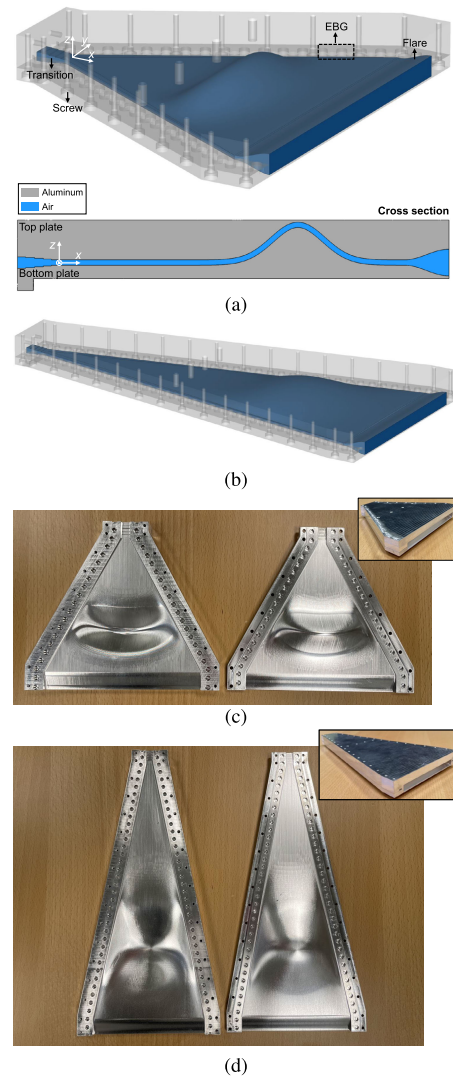

Fig. 11. (a) Full-wave (CST) model of design I and the cross section at the xz-plane, including the waveguide transition, radiation flare, and EBG structure. (b) Full-wave (CST) model of design II. Inside views of the two parts of the prototype: (c) design I and (d) design II (left: top plate, right: bottom plate, and inset: assembled horn).

In Fig. 11(a), the geometrical structure of design I is plotted. The design consists of two metallic plates that create a thin air channel for electromagnetic waves to propagate. The two parts were manufactured separately and then assembled with screws. To prevent possible leakages that occur in the gap between the two plates, an electromagnetic band gap (EBG) region is added to both sides of the horn, made up of glide-symmetric holes [41], [42]. Note that design II uses the same waveguide transition, radiation flare, and EBG structure as design I. The prototypes were manufactured by computerized numerical control (CNC) machining in aluminum (Al), as presented in Fig. 11(c) and (d). Some surface roughness can be observed on the inner surfaces of the prototypes and is expected to increase the insertion losses in K_a-band. Other manufacturing techniques, such as metallic additive manufacturing, are also possible, as demonstrated in [43].

C. Simulation and Experimental Validation

In this section, we show the results of full-wave (CST) simulations and measurements, including reflection coefficients,
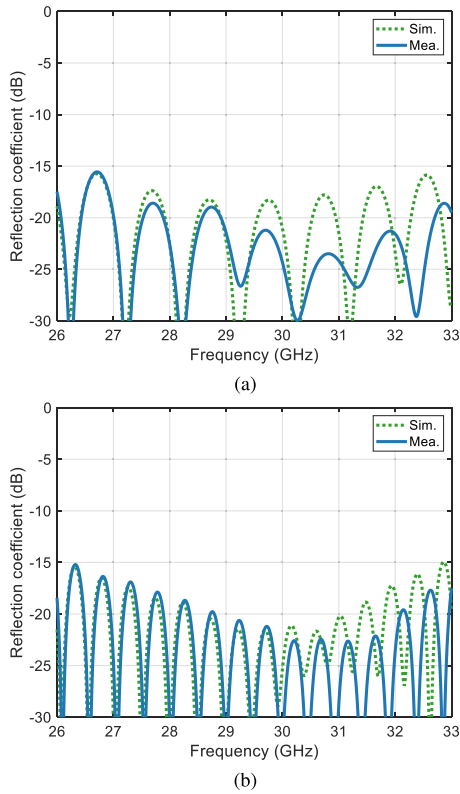
Fig. 12. Simulated and measured reflection coefficient of (a) design I and (b) design II.
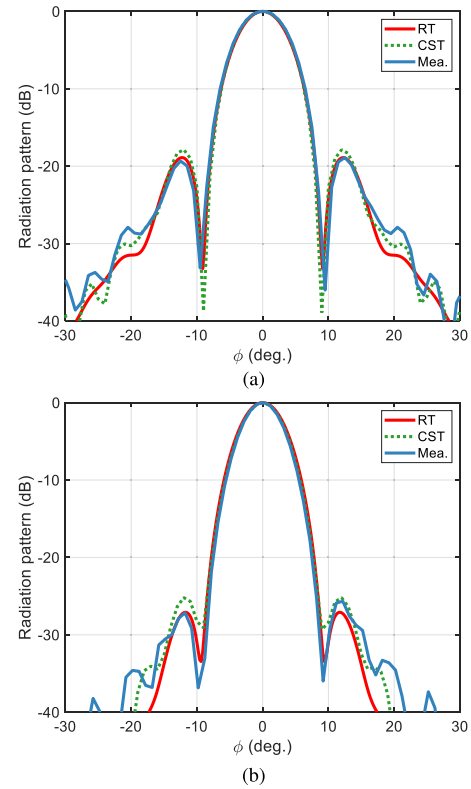

Fig. 13. Comparison of the radiation patterns obtained with various methods for (a) design I and (b) design II in the beamforming plane at 30 GHz.

Fig. 14. Realized gain patterns of design I over frequency in the beamforming plane. (a) Simulated results (CST). (b) Measured results.

radiation patterns, realized gains, and aperture efficiencies. The simulated and measured reflection coefficients for designs I and II are reported in Fig. 12(a) and (b). The simulated and measured results of both horns are smaller than −15 dB in the entire operating frequency range from 26 to 33 GHz. Note that time gating was used to eliminate the influence of the adapter and the surrounding environment on the measurements.

To obtain far-field characteristics, the antenna prototypes were measured in the anechoic chamber at KTH in a far-field setup, with a standard-gain horn antenna used as the probe. The radiation patterns provided by the RT model, the CST model, and the measurement for both designs at 30 GHz are plotted in Fig. 13. The RT tool predicts the shape of the main beam very well in both cases. Some deviations can be observed in the sidelobes, although they are acceptable given that they occur at values below −20 dB.

The realized gain patterns of designs I and II are compared in Figs. 14 and 15, including simulation and measured data in the frequency range 26–33 GHz. The simulation and measured results agree well with each other for both designs, demonstrating good frequency stability of the focusing properties. Furthermore, low sidelobe levels lower than −15 dB for design I and −25 dB for design II are obtained within the working frequency range. The frequency behavior of the realized gain and the aperture efficiency of both designs are compared in Figs. 16 and 17. The aperture efficiency is calculated by comparing the realized gain with the gain of a rectangular reference aperture with a height of 10 mm and a width of $2R \sin \phi_0$ (150 mm for design I and 124.7 mm for design II), assuming a uniform E-field distribution. To understand the

deviation between measurement and full-wave simulation, two different materials are used to model the metal plates in the CST simulation, the red dashed lines representing the PEC results and the red solid lines those of lossy Al with
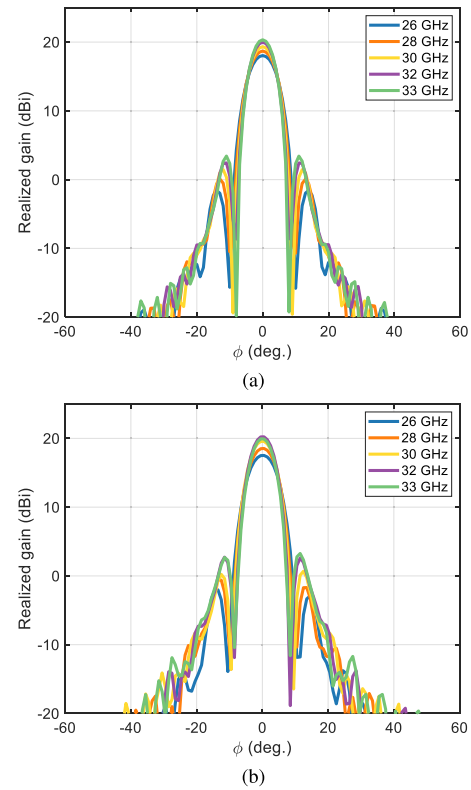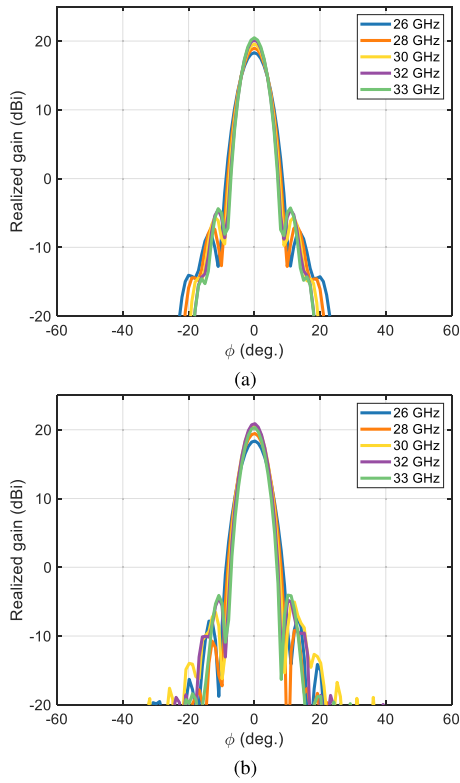
Fig. 15. Realized gain patterns of design II over frequency in the beamforming plane. (a) Simulated results (CST). (b) Measured results.
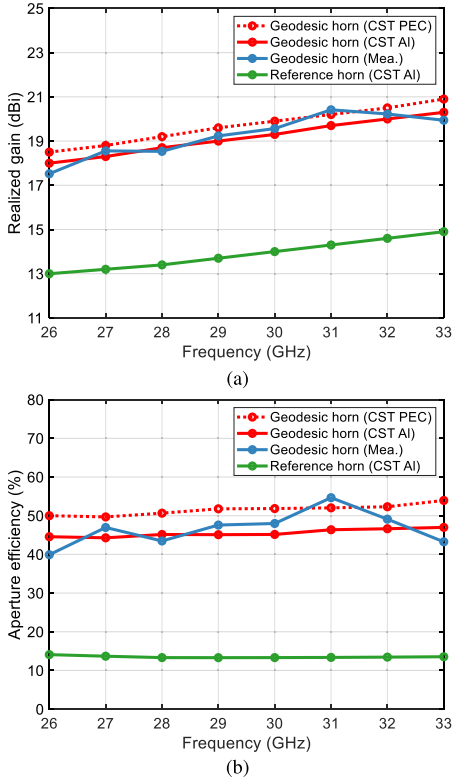

Fig. 17. (a) Realized gain and (b) aperture efficiency versus frequency of design II and the reference horn.

Fig. 16. (a) Realized gain and (b) aperture efficiency versus frequency of design I and the reference horn.

an electric conductivity of 3.56×10^7 S/m and a root-mean-square surface roughness of $3\,\mu$m (which is a realistic approximation of the manufacturing material [38]). For comparison purpos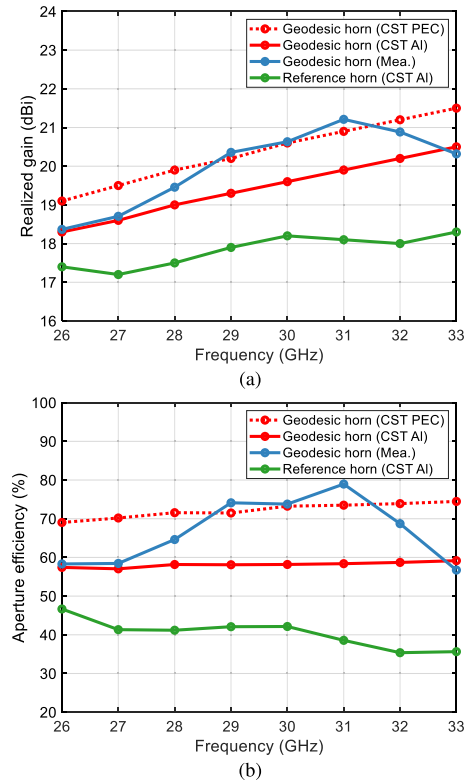es, the results of the planar reference horns, assuming plates made up of Al, are plotted in green in the figures. The reference horns have the same dimension parameters R and ϕ_0, as well as the same transition and flare as the geodesic horns. Regarding design I in Fig. 16, the measured results fall mainly in or close to the simulation range, with some deviations caused mainly by manufacturing and measurement errors. Compared to the reference horn, design I achieves a significant increase in gain of more than 5 dB from 26 to 33 GHz. The aperture efficiency of design I is around 45%, while that of the reference horn is less than 15%. Most importantly, design I does not increase the in-plane dimensions, with a total height of only 22 mm. Although slightly higher than the reference horn (12 mm in height), this design is still very compact. Regarding design II in Fig. 17, the deviations between measurement and simulation occur mainly in the frequency range from 29 to 31 GHz, most likely due to manufacturing errors. The measured aperture efficiency is around 70% from 28 to 32 GHz and 60% at other frequencies, compared to around 40% for the simulation results of the reference horn. Similar to design I, the total height of design II is 23 mm, which is slightly higher than the 12 mm of the reference horn. In fact, the height profile could be reduced by introducing a folded profile, which has been proven by modulated geodesic lenses [4], [44]. Taking into account the improved performance compared to planar reference horn antennas, the reported geodesic H-plane horn antennas are promising as high-efficiency beamformers. Finally, we summarize the main performances of this development in Table III and compare them to other H-plane horn antennas, highlighting that the proposed concept has the advantage of wideband operation and high realized gain and efficiency.

TABLE III
COMPARISON OF H-PLANE HORN DESIGNS

Reference	Applied technology	Freq. bandwidth	Realized gain	Increased gain	SLL	Aper. eff.	Total eff.
[10]	Dielectric loaded SIW	27 GHz	9.3 dBi @ 27 GHz	≈ 6 dB	-10 dB	N/A	57.8%
[14]	Gap SIW	$31 \sim 39$ GHz	10.3 dBi @ 34 GHz	> 6 dB	-10 dB	N/A	N/A
[17]	Holey SIW	$34.3 \sim 44.5$ GHz	12 dBi @ 40 GHz	2.3 dB	-20 dB	$45 \sim 60\%$	$\approx 76\%$
[19]	Metal-via SIW	$28 \sim 36.5$ GHz	7.87 dBi @ 35.5 GHz	$1 \sim 4$ dB	$-10 \sim -2$ dB	N/A	$\approx 90\%$
[23]	Slow-wave structures	$10.5 \sim 14.5$ GHz	$9.3 \sim 11.8$ dBi	1.7 dB	-10 dB	$65 \sim 80\%$	N/A
Design I	Geodesic horn	$26 \sim 33$ GHz	19.6 dBi @ 30 GHz	> 5 dB	< -15 dB	$\approx 45\%$	$> 85\%$
Design II	Geodesic horn	$26 \sim 33$ GHz	20.6 dBi @ 30 GHz	$1 \sim 2$ dB	< -25 dB	$\approx 65\%$	$> 75\%$

IV. CONCLUSION

This article proposes the novel concept of geodesic H-plane horn antennas. In this new type of horn antenna, the phase properties are tuned by using a geodesic shape. Additionally, we propose a numerical method based on a ray-tracing approach to efficiently compute triangular surfaces that define geodesic H-plane horn antennas. With the aim of correcting phase errors of conventional H-plane horns, we conceived a height profile with a Gaussian and a quasicosine distribution along the ρ- and ϕ-directions. The specific parameters of the height profile were optimized using the proposed numerical method for two different horn configurations, the so-called designs I and II. This numerical method was satisfactorily validated by comparing its results with the full-wave simulation data and the measured results. The geodesic H-plane horn antennas operate from 26 to 33 GHz with a reflection coefficient below -15 dB in both simulations and measurements. Design I realizes an increased gain of over 5 dB when compared to a planar reference horn, while design II has an aperture efficiency of around 65%. Good agreement was found between the simulation and the experimental results, both in terms of the reflection coefficient and the radiation patterns. Being simple, compact, and highly efficient, this beamformer solution has the potential to become a possible candidate for high-frequency antennas.

ACKNOWLEDGMENT

REFERENCES

[1] O. Quevedo-Teruel, M. Ebrahimpouri, and F. Ghasemifard, "Lens antennas for 5G communications systems," *IEEE Commun. Mag.*, vol. 56, no. 7, pp. 36–41, Jul. 2018.

[2] Y. J. Guo, M. Ansari, R. W. Ziolkowski, and N. J. G. Fonseca, "Quasi-optical multi-beam antenna technologies for B5G and 6G mmWave and THz networks: A review," *IEEE Open J. Antennas Propag.*, vol. 2, pp. 807–830, Jun. 2021.

[3] P. S. Hall and S. J. Vetterlein, "Review of radio frequency beamforming techniques for scanned and multiple beam antennas," *IEE Proc. H-Microw., Antennas Propag.*, vol. 137, pp. 293–303, Oct. 1990.

[4] O. Quevedo-Teruel et al., "Geodesic lens antennas for 5G and beyond," *IEEE Commun. Mag.*, vol. 60, no. 1, pp. 40–45, Jan. 2022.

[5] R. F. Rinehart, "A solution of the problem of rapid scanning for radar antenna," *J. Appl. Phys.*, vol. 19, no. 9, pp. 860–862, Sep. 1948.

[6] Q. Chen, S. A. R. Horsley, N. J. G. Fonseca, T. Tyc, and O. Quevedo–Teruel, "Double-layer geodesic and gradient-index lenses," *Nature Commun.*, vol. 13, no. 1, pp. 1–12, Apr. 2022.

[7] C. A. Balanis, *Antenna Theory: Analysis and Design*, 4th ed. Hoboken, NY, USA: Wiley, 2016.

[8] M. Quddus and J. German, "Phase correction by dielectric slabs in sectoral horn antennas," *IRE Trans. Antennas Propag.*, vol. AP-9, no. 4, pp. 413–415, Jul. 1961.

[9] W. E. Kock, "Metal-lens antennas," *Proc. IRE*, vol. 34, no. 11, pp. 828–836, Nov. 1946.

[10] H. Wang, D.-G. Fang, B. Zhang, and W.-Q. Che, "Dielectric loaded substrate integrated waveguide (SIW) H-plane horn antennas," *IEEE Trans. Antennas Propag.*, vol. 58, no. 3, pp. 640–647, Mar. 2010.

[11] K. Iigusa, K. Li, K. Sato, and H. Harada, "Gain enhancement of H-plane sectoral post-wall horn antenna by connecting tapered slots for millimeter-wave communication," *IEEE Trans. Antennas Propag.*, vol. 60, no. 12, pp. 5548–5556, Dec. 2012.

[12] H. Jamshidi-Zarmehri and M. H. Neshati, "Design and development of high-gain SIW H-plane horn antenna loaded with waveguide, dipole array, and reflector nails using thin substrate," *IEEE Trans. Antennas Propag.*, vol. 67, no. 4, pp. 2813–2818, Apr. 2019.

[13] Y. Oh, N. Kordsmeier, H. Askari, and J. J. Adams, "Low profile GRIN lenses with integrated matching using 3-D printed ceramic," *IEEE Open J. Antennas Propag.*, vol. 4, pp. 12–22, 2023.

[14] L. Wang, M. Esquius-Morote, H. Qi, X. Yin, and J. R. Mosig, "Phase corrected H-plane horn antenna in gap SIW technology," *IEEE Trans. Antennas Propag.*, vol. 65, no. 1, pp. 347–353, Jan. 2017.

[15] N. Bayat-Makou and A. A. Kishk, "Substrate integrated horn antenna with uniform aperture distribution," *IEEE Trans. Antennas Propag.*, vol. 65, no. 2, pp. 514–520, Feb. 2017.

[16] H. Eskandari, J. L. Albadalejo-Lijarcio, O. Zetterstrom, T. Tyc, and O. Quevedo-Teruel, "H-plane horn antenna with enhanced directivity using conformal transformation optics," *Sci. Rep.*, vol. 11, no. 1, p. 14322, Jul. 2021.

[17] A. Biedma-Pérez, P. Padilla, C. Segura-Gómez, and Á. Palomares-Caballero, "Holey SIW horn antenna based on an H-plane lenswise wavefront collimation," *IEEE Trans. Antennas Propag.*, vol. 71, no. 1, pp. 1023–1028, Jan. 2023.

[18] Z. Gholipour and J. Ahmadi-Shokouh, "Substrate integrated waveguide corrugated horn antenna," *Wireless Pers. Commun.*, vol. 109, no. 3, pp. 1605–1614, Aug. 2019.

[19] L. Wang, X. Yin, S. Li, H. Zhao, L. Liu, and M. Zhang, "Phase corrected substrate integrated waveguide H-plane horn antenna with embedded metal-via arrays," *IEEE Trans. Antennas Propag.*, vol. 62, no. 4, pp. 1854–1861, Apr. 2014.

[20] Y. Zhang, J. Deng, D. Sun, J. Yin, and L. Guo, "Compact slow-wave SIW H-plane horn antenna with increased gain for vehicular millimeter wave communication," *IEEE Trans. Veh. Technol.*, vol. 70, no. 7, pp. 7289–7293, Jul. 2021.

[21] A. Araghi, M. Khalily, O. Yurduseven, P. Xiao, and R. Tafazolli, "Guided-wave manipulation in SIW H-plane horn antenna by combining phase correction and holographic-based leakage," *Sci. Rep.*, vol. 12, no. 1, pp. 1–13, Jul. 2022.

[22] D. Sun and J. Xu, "Compact phase corrected H-plane horn antenna using slow-wave structures," *IEEE Antennas Wireless Propag. Lett.*, vol. 16, pp. 1032–1035, 2017.

[23] J. Deng et al., "Horn antenna with miniaturized size and increased gain by loading slow wave periodic metal blocks," *IEEE Trans. Antennas Propag.*, vol. 69, no. 4, pp. 2365–2369, Apr. 2021.

[24] A. Rolland, M. Ettorre, M. Drissi, L. Le Coq, and R. Sauleau, "Optimization of reduced-size smooth-walled conical horns using BoR-FDTD and genetic algorithm," *IEEE Trans. Antennas Propag.*, vol. 58, no. 9, pp. 3094–3100, Sep. 2010.

[25] A. Rolland, N. T. Nguyen, R. Sauleau, C. Person, and L. Le Coq, "Smooth-walled light-weight Ka-band shaped horn antennas in metallized foam," *IEEE Trans. Antennas Propag.*, vol. 60, no. 3, pp. 1245–1251, Mar. 2012.

[26] A. Rolland, A. V. Boriskin, C. Person, C. Quendo, L. Le Coq, and R. Sauleau, "Lens-corrected axis-symmetrical shaped horn antenna in metallized foam with improved bandwidth," *IEEE Antennas Wireless Propag. Lett.*, vol. 11, pp. 57–60, Jan. 2012.

[27] N. J. G. Fonseca, Q. Liao, and O. Quevedo-Teruel, "Equivalent planar lens ray-tracing model to design modulated geodesic lenses using non-Euclidean transformation optics," *IEEE Trans. Antennas Propag.*, vol. 68, no. 5, pp. 3410–3422, May 2020.

[28] Q. Liao, N. J. G. Fonseca, M. Camacho, Á. Palomares-Caballero, F. Mesa, and O. Quevedo-Teruel, "Ray-tracing model for generalized geodesic-lens multiple-beam antennas," *IEEE Trans. Antennas Propag.*, vol. 71, no. 3, pp. 2640–2651, Mar. 2023.

[29] F. Doucet, N. J. G. Fonseca, E. Girard, H. Legay, and R. Sauleau, "Analytical model and study of continuous parallel plate waveguide lens-like multiple-beam antennas," *IEEE Trans. Antennas Propag.*, vol. 66, no. 9, pp. 4426–4436, Sep. 2018.

[30] F. Doucet et al., "Shaped continuous parallel plate delay lens with enhanced scanning performance," *IEEE Trans. Antennas Propag.*, vol. 67, no. 11, pp. 6695–6704, Nov. 2019.

[31] T. Ströber, S. Tubau, E. Girard, H. Legay, G. Goussetis, and M. Ettorre, "Shaped parallel-plate lens for mechanical wide-angle beam steering," *IEEE Trans. Antennas Propag.*, vol. 69, no. 12, pp. 8158–8169, Dec. 2021.

[32] F. Doucet, N. J. G. Fonseca, E. Girard, X. Morvan, and R. Sauleau, "Compact planar beamformer using multiple continuous parallel-plate waveguide delay lenses," *IEEE Antennas Wireless Propag. Lett.*, vol. 21, no. 11, pp. 2229–2233, Nov. 2022.

[33] S. Yang, Q. Chen, F. Mesa, N. J. G. Fonseca, and O. Quevedo-Teruel, "Geodesic half-maxwell fish-eye-lens antenna," *IEEE Trans. Antennas Propag.*, vol. 71, no. 3, pp. 2330–2338, Mar. 2023.

[34] Q. Liao, N. J. G. Fonseca, and O. Quevedo-Teruel, "Compact multibeam fully metallic geodesic Luneburg lens antenna based on non-Euclidean transformation optics," *IEEE Trans. Antennas Propag.*, vol. 66, no. 12, pp. 7383–7388, Dec. 2018.

[35] N. J. G. Fonseca, Q. Liao, and O. Quevedo-Teruel, "Compact parallel-plate waveguide half-Luneburg geodesic lens in the Ka-band," *IET Microw., Antennas Propag.*, vol. 15, no. 2, pp. 123–130, Feb. 2021.

[36] O. Orgeira, G. León, N. J. G. Fonseca, P. Mongelos, and O. Quevedo-Teruel, "Near-field focusing multibeam geodesic lens antenna for stable aggregate gain in far-field," *IEEE Trans. Antennas Propag.*, vol. 70, no. 5, pp. 3320–3328, May 2022.

[37] F. V. Vidarsson et al., "Conformal parallel plate waveguide polarizer integrated in a geodesic lens antenna," *IEEE Trans. Antennas Propag.*, vol. 70, no. 11, pp. 10327–10337, Nov. 2022.

[38] P. Castillo-Tapia et al., "Two-dimensional beam steering using a stacked modulated geodesic Luneburg lens array antenna for 5G and beyond," *IEEE Trans. Antennas Propag.*, vol. 71, no. 1, pp. 487–496, Jan. 2023.

[39] O. Zetterstrom, M. Petek, P. Castillo-Tapia, Á. Palomares-Caballero, N. J. G. Fonseca, and O. Quevedo-Teruel, "V-band fully metallic geodesic Luneburg lens antenna," *IEEE Trans. Antennas Propag.*, vol. 71, no. 2, pp. 1965–1970, Feb. 2023.

[40] C. Zhu, R. H. Byrd, P. Lu, and J. Nocedal, "Algorithm 778: L-BFGS-B: Fortran subroutines for large-scale bound-constrained optimization," *ACM Trans. Math. Softw.*, vol. 23, no. 4, pp. 550–560, Dec. 1997.

[41] M. Ebrahimpouri, E. Rajo-Iglesias, Z. Sipus, and O. Quevedo-Teruel, "Cost-effective gap waveguide technology based on glide-symmetric holey EBG structures," *IEEE Trans. Microw. Theory Techn.*, vol. 66, no. 2, pp. 927–934, Feb. 2018.

[42] O. Quevedo-Teruel, Q. Chen, F. Mesa, N. J. G. Fonseca, and G. Valerio, "On the benefits of glide symmetries for microwave devices," *IEEE J. Microw.*, vol. 1, no. 1, pp. 457–469, Jan. 2021.

[43] J. Rico-Fernández, F. V. Vidarsson, M. Arrebola, N. J. G. Fonseca, and O. Quevedo-Teruel, "Compact and lightweight additive manufactured parallel-plate waveguide half-Luneburg geodesic lens multiple-beam antenna in the Ka-band," *IEEE Antennas Wireless Propag. Lett.*, vol. 22, no. 4, pp. 684–688, Apr. 2023.

[44] K. S. Kunz, "Propagation of microwaves between a parallel pair of doubly curved conducting surfaces," *J. Appl. Phys.*, vol. 25, no. 5, pp. 642–653, May 1954.

Mingzheng Chen (Student Member, IEEE) received the B.Sc. and M.Sc. degrees from Southeast University, Nanjing, China, in 2018 and 2021, respectively. He is currently pursuing the Ph.D. degree with the Division of Electromagnetic Engineering and Fusion Science, School of Electrical Engineering and Computer Science, KTH Royal Institute of Technology, Stockholm, Sweden.

His current research interests include lens antennas.

Francisco Mesa (Fellow, IEEE) received the Licenciado and Ph.D. degrees in physics from the Universidad de Sevilla, Seville, Spain, in 1989 and 1991, respectively.

He is currently a Professor with the Departamento de Física Aplicada 1, Universidad de Sevilla. His research interests include electromagnetic propagation/radiation in microwave and quasi-optical structures.

Oscar Quevedo-Teruel (Fellow, IEEE) received the Telecommunication Engineering and Ph.D. degrees from the Carlos III University of Madrid, Madrid, Spain, in 2005 and 2010, respectively.

From 2010 to 2011, he was with the Department of Theoretical Physics of Condensed Matter, Universidad Autonoma de Madrid, Madrid, as a Research Fellow, and went on to continue his post-doctoral research at the Queen Mary University of London, London, U.K., from 2011 to 2013. In 2014, he joined the Division of Electromagnetic Engineering and Fusion Science, School of Electrical Engineering and Computer Science, KTH Royal Institute of Technology, Stockholm, Sweden, where he is currently a Professor and the Director of the Master Programme in Electromagnetics Fusion and Space Engineering. He has made scientific contributions to higher symmetries, transformation optics, lens antennas, metasurfaces, and high-impedance surfaces. He is the coauthor of more than 120 articles in international journals and 200 papers at international conferences.

Dr. Quevedo-Teruel was the EurAAP Delegate for Sweden, Norway, and Iceland, from 2018 to 2020, and he has been a member of the EurAAP Board of Directors since January 2021. Since January 2022, he has been the Vice-Chair of EurAAP. He was a Distinguished Lecturer of the IEEE Antennas and Propagation Society from 2019 to 2021. He has been the Chair of the IEEE APS Educational Initiatives Programme since 2020. He has been an Associate Editor of the IEEE TRANSACTIONS ON ANTENNAS AND PROPAGATION from 2018 to 2022 and a Track Editor since 2022. He has been the Founder and the Editor-in-Chief of the *EurAAP Journal Reviews of Electromagnetics* since 2020.